



# Interfacial modulation of $\text{ZnIn}_2\text{S}_4$ with high active Zr- $\text{S}_4$ sites for boosting photocatalytic activation of oxygen and degradation of emerging contaminant

Hui Li<sup>a</sup>, Haodong Ji<sup>b</sup>, Jiajia Liu<sup>a</sup>, Wen Liu<sup>b,\*</sup>, Fan Li<sup>b</sup>, Zhurui Shen<sup>a,\*</sup>

<sup>a</sup> School of Materials Science and Engineering and Smart Sensing Interdisciplinary Science Center, Nankai University, Tianjin 300350, China

<sup>b</sup> College of Environmental Sciences and Engineering, Peking University, Beijing 100871, China

## ARTICLE INFO

### Keywords:

Interfacial modulation

Photocatalysis

$\text{ZrS}_4$  active sites

$\text{O}_2$  activation

Emerging contaminant

## ABSTRACT

Interfacial modulation of catalysts for constructing active sites can greatly promote its catalytic activity, while the mechanism on reactive species production at different interfaces still needs to be revealed. In this study,  $\text{Zr-S}_4$  active sites were usefully constructed on  $\text{ZnIn}_2\text{S}_4$  nanosheets, which effectively modulated the reaction interface and band structure, thus boosting the photocatalytic activity. The optimized material ( $\text{Zr}_{1.2}\text{-ZIS}$ ) showed a ~3-fold kinetic rate constant for photocatalytic degradation of tetracycline compared with the pristine  $\text{ZnIn}_2\text{S}_4$ . Moreover, TC underwent a different degradation pathway over the modified catalyst due to regulation of reactive species after photo-activation. The  $\text{Zr-S}_4$  centers were energetically favorable for activating  $\text{O}_2$  into  $\bullet\text{O}_2$  and  $\bullet\text{OH}$ , as a more reactive d-band electron was obtained and the adsorption of  $\bullet\text{O}_2$  as well as its further conversion into  $\bullet\text{OH}$  was promoted. Theoretical calculations on Fukui index and toxicity also confirmed the dramatical toxicity reduction during TC degradation by  $\text{Zr}_{1.2}\text{-ZIS}$ .

## 1. Introduction

Tetracycline (TC) is a broad-spectrum antibiotic widely used in human treatment, animal husbandry and agriculture. [1,2] The excessive use and emission of TC have high ecotoxicity and environmental durability, leading to environmental pollution hard to be treated, [3] which is challenging to develop new catalysts to achieve the highly efficient degradation and toxicity decreasing for the control of antibiotics in waters. Interfacial modulation such as construction of a heterojunction, [4] incorporation of cocatalysts [5] and introduction of single atoms and clusters [6] can effectively regulate the energy band structure, promote charge transfer and further improve the photocatalytic activity. [7] Recently, monatomic and cluster supported on classical photocatalysts to modulate the electronic and band structures for boosting photocatalytic activity has attracted intensive attention. [8,9] For photocatalytic degradation of contaminants in the environmental clean-up area, suitable monatomic or cluster centers are found to better adsorb reactants than bulk materials, thus promote electron exchange between catalysts and reactants. In addition, they also can better activate precursors (e.g., molecular oxygen) for reactive oxygen species (ROS) production. Specifically, single-atom architecture on catalysts generally

can increase electron density, and then promote charge transfer and separation. [10] For example, metal single-atom has much better ability for activating  $\text{O}_2$  for ROS production due to formation of metal-O intermediate species. [11] Previously, we developed a Ag single atomic catalyst, which could greatly promote electron transfer, boost the  $\text{O}_2$  activation and enhance the degradation of TC. [6] Therefore, mono-atomic and cluster centers have great potential for highly efficient generating ROS and contaminants degradation. Moreover, rational design of novel catalytic centers at single atomic or cluster scale would provide new opportunities for regulating the types of produced ROS, thus achieving reaction pathways and transformation products/intermediates control during degradation of contaminants.

$\text{O}_2$  is a green, economical and rich oxidant, which can be activated into ROS during photocatalysis. Among many kinds of state-of-art candidates,  $\text{ZnIn}_2\text{S}_4$  (ZIS) is selected here for photocatalytic activation of  $\text{O}_2$  due to its specific band energy structures. The photogenerated electrons ( $e^-$ ) in conduction band (CB) of ZIS ( $-0.49$  eV vs. NHE) can efficiently reduce  $\text{O}_2$  to produce  $\bullet\text{O}_2$  ( $E(\text{O}_2/\bullet\text{O}_2) = -0.33$  eV vs. NHE) due to its much negative CB position. [12] However, the photogenerated holes ( $h^+$ ) in valence band (VB) of ZIS ( $1.69$  eV vs. NHE) cannot oxidize  $\text{H}_2\text{O}$  ( $E(\bullet\text{OH}/\text{H}_2\text{O}) = 2.38$  eV vs. NHE) or  $\text{OH}^-$  ( $E(\bullet\text{OH}/\text{OH}^-) = 2.72$  eV vs.

\* Corresponding authors.

E-mail addresses: [wen.liu@pku.edu.cn](mailto:wen.liu@pku.edu.cn) (W. Liu), [shenzhurui@nankai.edu.cn](mailto:shenzhurui@nankai.edu.cn) (Z. Shen).

<https://doi.org/10.1016/j.apcatb.2023.122481>

Received 30 September 2022; Received in revised form 1 February 2023; Accepted 15 February 2023

Available online 16 February 2023

0926-3373/© 2023 Elsevier B.V. All rights reserved.

NHE) to  $\bullet\text{OH}$  due to its low VB energy.[13] In addition, ZIS is a  $\text{AB}_2\text{X}_4$  family semiconductor, containing alternate stacking structure of  $\text{S}-\text{Zn}-\text{S}-\text{In}-\text{S}-\text{In}-\text{S}$ , which can be well tailored through introduction of other metal atoms.[14] In addition, ZIS also has several other fascinating advantages, such as good physicochemical stability, low toxicity and facile synthesis method.[15] Especially, due to its layered nanostructure, it exhibits versatility in interface modulation,[16] such as vacancy engineering,[17–20] doping engineering[21–23] and construction of heterojunction.[24–26] Zr–S active sites are designed to construct on the interface of ZIS, because it can well regulate the electronic and band structures of ZIS, and also can improve adsorption of  $\text{O}_2$  and target contaminant at the interface. Meanwhile, the highly positive charged Zr–S active sites can regulate the proportion and yield of ROS, so as to change the degradation pathway of contaminant.

In these regards, highly positive charged Zr– $\text{S}_4$  active sites were introduced on the surface of  $\text{ZnIn}_2\text{S}_4$  nanosheets (Zr $\text{S}_4$ -ZIS) in this work. A typical emerging organic contaminant, TC was selected as the target contaminant to evaluate the photocatalytic activity of Zr $\text{S}_4$ -ZIS with different Zr (in Zr– $\text{S}_4$ ) amounts. Materials characterizations including X-ray absorption fine structure (XAFS) analysis was conducted to analyze the coordination environment of Zr, while theoretical calculations based on density functional theory (DFT) were applied to reveal the ROS formation mechanism at the interface of Zr– $\text{S}_4$  active sites and  $\text{ZnIn}_2\text{S}_4$ . In addition, the degradation intermediates and products were carefully identified in both Zr $\text{S}_4$ -ZIS and pristine  $\text{ZnIn}_2\text{S}_4$  systems, and moreover, the degradation pathway and toxicity evolution of products were compared. This study provides an available method on interfacial engineering construction of single atomic and cluster scale catalysts, which can be applied for efficient emerging contaminants degradation along with toxicity reduction in water.

## 2. Materials and methods

### 2.1. Fabrication of Zr $\text{S}_4$ -ZIS catalysts

The chemicals and reagents used in this study are presented in Text S1 of Supplementary Material. The  $\text{ZnIn}_2\text{S}_4$  and  $\text{Zr}_x\text{-ZnIn}_2\text{S}_4$  nanosheets were synthesized by a facile hydrothermal method.[8,23] Typically, 0.8 mmol  $\text{Zn}(\text{CH}_3\text{COO})_2 \cdot 2\text{H}_2\text{O}$ , 6.4 mmol thioacetamide, 1.6 mmol  $\text{InCl}_3 \cdot 4\text{H}_2\text{O}$  and a certain amount of  $\text{ZrCl}_4$  (0, 0.02, 0.06 and 0.2 mmol) were added into a mixed solution (30 mL water + 30 mL ethanol), which was then stirred vigorously for 30 min. Subsequently, the mixed solution was moved to a 100 mL Teflon-lined stainless steel autoclave and heated for 24 h at 180 °C. After cooled down to the room temperature, the sample was collected by washing with distilled water and ethanol, and dried in an oven overnight at 60 °C. The Zr content (wt%) in Zr $\text{S}_4$ -ZIS was determined by an inductively coupled plasma mass spectrometry (ICP-MS, X7 Series, Thermo Electron Corporation, USA) after the material was totally dissolved in acid.[23] According to the detected Zr amount (Table S1), the obtained materials were labeled as ZIS, Zr $_{0.4}$ -ZIS, Zr $_{1.2}$ -ZIS and Zr $_{4.5}$ -ZIS, respectively. Material characterization methods are shown in Text S2. The transient photocurrent and electrochemical impedance spectra (EIS) of material were also measured (Text S3).

### 2.2. Photocatalytic performance evaluation and TC degradation

The photocatalytic performance of all the synthesized catalysts were evaluated by TC degradation. Specifically, the TC photocatalytic degradation experiments were performed in a quartz reactor (total volume of 100 mL) under light irradiation. A 300 W xenon lamp with a 420 nm UV cut-off filter and an intensity of 135 mW/cm<sup>2</sup> was placed at a 38 cm distance over the reactor. 25 mg catalyst was added into 50 mL TC solution with initial concentration of 20 mg/L, and solution pH was adjusted to  $7.0 \pm 0.2$  using diluted NaOH (0.5 M) or  $\text{HClO}_4$  (0.5 M). Circulating water was injected to maintain the reaction temperature of 25 °C. Subsequently, the mixed solution was stirred to achieve the

adsorption-desorption equilibrium for 1 h in dark. Afterwards, the xenon lamp was turned on to initialize the reaction. 2 mL reaction solution was taken at specific intervals and mixed with 2 mL NaOH (0.1 M) for extraction all the TC in sample (recovery rate >95%), and then immediately flited through a 0.22  $\mu\text{m}$  syringe-membrane. The TC concentration in the filtrate was determined on an Agilent 1260 Infinity high performance liquid chromatography (HPLC, Agilent, USA), and the transformation products (TPs) of TC were analyzed on an Ultimate 3000 ultra-HPLC (UHPLC, Dionex, USA) equipped with Orbitrap Fusion Tri-brid mass spectrometer (Thermo Scientific, USA). The detailed analytical methods on TC and TPs are shown in Text S4. Total organic carbon (TOC) was detected on TOC-VCPH (Shimadzu, Japan) analyzer. Dissolved oxygen (DO) in solution was measured by an AR8010 dissolved oxygen meter (Smart Sensor, China).

The first-order reaction kinetics model (Eq. 1) was used to describe the degradation kinetics of TC:[27].

$$\ln(C_0/C_t) = -k_1 t \quad (1)$$

where  $C_0$  and  $C_t$  (mg/L) are the concentrations at initial and reaction time  $t$  (min), respectively;  $k_1$  ( $\text{min}^{-1}$ ) is the reaction rate constant.

### 2.3. ROS identification and contributions evaluation

Electron spin resonance (ESR) were recorded on a Bruker A300 spectrometer (Bruker, Germany) to identified the produced ROS during photocatalysis after trapped by 5,5-dimethyl-1-pyrroline  $N$ -oxide (DMPO). Then, the scavenger quenching tests were carried out in the same way as the photocatalytic degradation of TC, except for adding capture reagents before irradiation. In addition, 1 mM ascorbic acid (AA),  $p$ -benzoquinone (PBQ) and isopropanol (IPA) were used to capture  $\text{h}^+$ ,  $\bullet\text{O}_2^-$ , or  $\bullet\text{OH}$ . The contributions of  $\bullet\text{OH}$ ,  $\bullet\text{O}_2^-$  and  $\text{h}^+$  to TC degradation were estimated according to the following equations:[13].

$$R_{\bullet\text{O}_2^-} = \frac{k_{\bullet\text{O}_2^-}}{k_0} \approx \frac{k_0 - k_{\text{PBQ}}}{k_0} \quad (2)$$

$$R_{\bullet\text{OH}} = \frac{k_{\bullet\text{OH}}}{k_0} \approx \frac{k_0 - k_{\text{IPA}}}{k_0} \quad (3)$$

$$R_{\text{h}^+} = \frac{k_{\text{h}^+}}{k_0} \approx \frac{k_0 - k_{\text{AA}}}{k_0} \quad (4)$$

in which  $R$  is the contribution proportion of specific reactive species;  $k_i$  is the reaction rate constant of  $\text{h}^+$ ,  $\bullet\text{O}_2^-$ , or  $\bullet\text{OH}$  or in the presence of AA, PBQ and IPA, respectively.

For the qualification of ROS during photocatalysis, the concentration of produced  $\bullet\text{O}_2^-$  was tested under light irradiation using  $2.5 \times 10^{-4}$  M nitroterazolium blue chloride as an indicating agent at a characteristic absorption wavelength of 259 nm.[7,28] The concentration of produced  $\bullet\text{OH}$  was measured by using 0.2 mM salicylic acid as an indicating agent at the characteristic absorption wavelength of 330 nm, detected by P4 UV–visible spectrophotometer (Shanghai MAPADA, China).[6].

### 2.4. Theoretical calculations

DFT calculations on material methods on ZIS and Zr $\text{S}_4$ -ZIS materials were performed on the Vienna ab initio package (VASP) 6.1.0 (details shown in Text S5). The information on reactive sites of TC was obtained from the Peking University Reactive Sites for Organic Compounds Database (PKU-REOD),[29,30] which was carried out on Gaussian 16 program (Revision C.01).[31] To balance the accuracy and duration during the geometry optimization and energy calculations, the theoretical level combined B3LYP method with the 6–31 +G(d,p) basis set was applied.[32] The solvent model based on self-consistent reaction field method was used to mimic the effect of water. Text S6 presents the theoretical calculations methods on Fukui index.

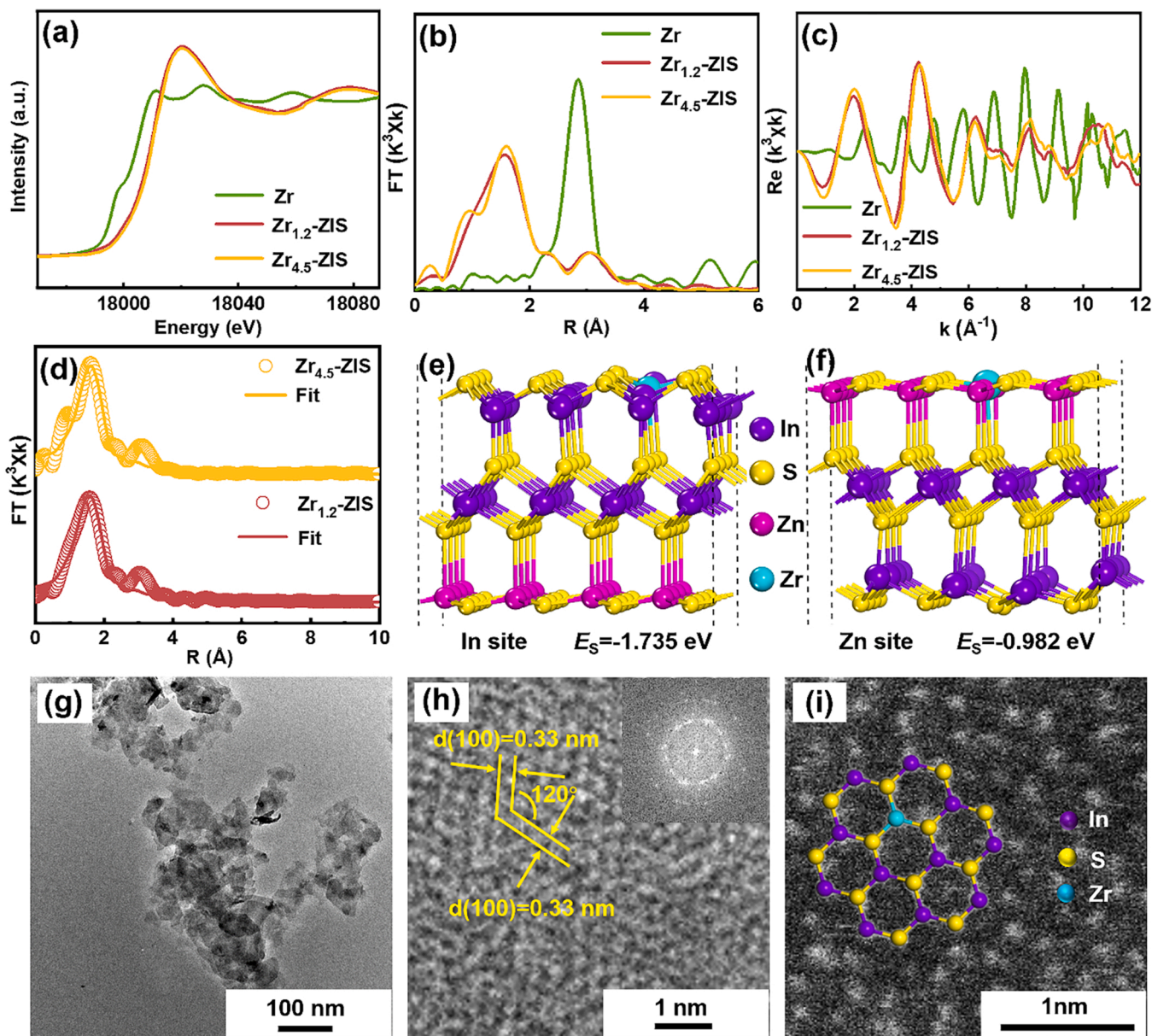


**Fig. 1.** (a) Zr K-edge XANES spectra of Zr<sub>1.2</sub>-ZIS and Zr<sub>4.5</sub>-ZIS compared with Zr foil standards; (b)  $k^3$ -weighted Fourier transforms EXAFS of Zr<sub>1.2</sub>-ZIS, Zr<sub>4.5</sub>-ZIS and Zr foil; (c) Zr K-edge extended EXAFS oscillation function of Zr<sub>1.2</sub>-ZIS, Zr<sub>4.5</sub>-ZIS and Zr foil; (d) EXAFS fitting results of Zr<sub>1.2</sub>-ZIS and Zr<sub>4.5</sub>-ZIS in  $r$  space; The formation energy of Zr atoms for substitution of (e) In and (f) Zn sites; (g) TEM image, (h) HRTEM image (inset: fast Fourier transform image) and (i) high-resolution STEM-HAADF image of Zr<sub>1.2</sub>-ZIS.

### 3. Results and discussion

#### 3.1. The structures, compositions and morphologies of catalysts

X-ray powder diffraction (XRD) patterns indicate the characteristic diffractions of all the synthesized materials (ZIS and various ZrS<sub>4</sub>-ZIS) are consistent with the hexagonal ZnIn<sub>2</sub>S<sub>4</sub> with  $P63mc$  space group (JCPDS 72-0773) (Fig.S1a). [17,33] No obvious impurity phase (e.g. ZrO<sub>2</sub>, ZrS<sub>2</sub>) is found after incorporation of Zr<sup>4+</sup>, revealing ZrS<sub>4</sub>-ZIS catalysts possess high purity and retain pristine crystal structure of ZIS. In order to study the chemical state of Zr atom, X-ray photoelectron spectroscopy (XPS) spectra of Zr 3d XPS are presented (Fig.S1c). The peaks of Zr 3d<sub>5/2</sub> (182.7 eV) and Zr 3d<sub>3/2</sub> (184.9 eV) are assigned to Zr<sup>4+</sup> species. Moreover, in Fig. S2, the peaks of Zr 3d<sub>5/2</sub> (182.7 eV) and Zr 3d<sub>3/2</sub> (184.9 eV) of Zr<sub>1.2</sub>-ZIS are significantly different from that of ZrS<sub>2</sub> (181.40 and 183.75 eV) and ZrO<sub>2</sub> (182.02 and 184.35 eV), indicating its

different coordination environment compared with ZrS<sub>2</sub> and ZrO<sub>2</sub>. [34].

To further study of chemical bonds and coordination environments of Zr atoms in different materials (i.e. Zr<sub>1.2</sub>-ZIS and Zr<sub>4.5</sub>-ZIS with higher Zr contents), X-ray absorption near edge structure (XANES) and extended X-ray absorption fine structure (EXAFS) are characterized to clarify the subtle atomic structures (Fig. 1). Fig. 1a indicates that all spectra of Zr foil, Zr<sub>1.2</sub>-ZIS and Zr<sub>4.5</sub>-ZIS exhibit a shoulder at around 18000 eV, corresponding to the pre-edge peak owing to the electric dipole-forbidden transition of the electron from 1 s to an unoccupied 4d orbital. [35] Moreover, the Zr K-edge of Zr<sub>1.2</sub>-ZIS and Zr<sub>4.5</sub>-ZIS is obviously shifted to a higher energy compared with Zr foil, indicating the species of Zr in Zr<sub>1.2</sub>-ZIS and Zr<sub>4.5</sub>-ZIS is Zr<sup>4+</sup> rather than metallic Zr<sup>0</sup>, consistent with the XPS results (Fig.S1c). The same results can be obtained in the Fourier transforms of EXAFS and Zr K-edge oscillation curves shown in Figs. 1b and 1c. The peak positions of Zr<sub>1.2</sub>-ZIS at  $\sim 1.59$  Å and Zr<sub>4.5</sub>-ZIS at  $\sim 1.60$  Å are attributed to the coordination



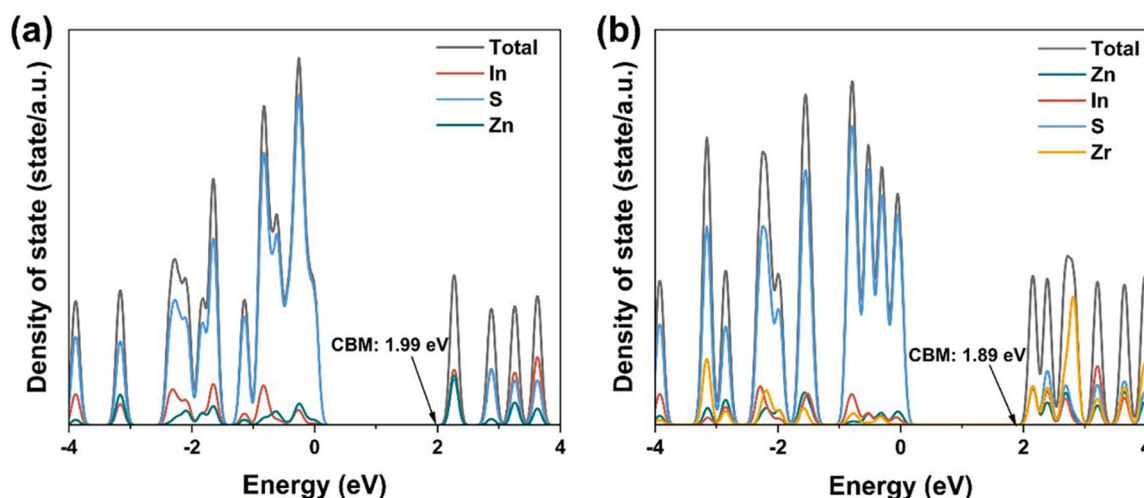


Fig. 2. Density of states (DOS) of (a) ZIS and (b)  $\text{Zr}_{1.2}\text{-ZIS}$  by DFT calculations.

between Zr and S (Fig. 1b), which are different from that of Zr foil at  $\sim 2.85$  Å assigned to Zr–Zr bond, suggesting the existence of Zr–S bonds while the absence of Zr–Zr bonds in these two  $\text{ZrS}_4\text{-ZIS}$  catalysts. Similarly, the Zr K-edge oscillation curves of  $\text{Zr}_{1.2}\text{-ZIS}$  and  $\text{Zr}_{4.5}\text{-ZIS}$  exhibit remarkable differences compared with that of Zr foil (Fig. 1c), also revealing the absence of Zr–Zr bond. In addition, the bond length of Zr–S in  $\text{Zr}_{1.2}\text{-ZIS}$  and  $\text{Zr}_{4.5}\text{-ZIS}$  are  $\sim 2.15$  and  $2.16$  Å in Table S2, respectively, which is close to the bond length of In–S ( $2.35$  Å) and Zn–S ( $2.36$  Å) in ZIS [14,36]. Therefore, Zr atoms substitute In and Zn sites to form a Zr–S bond after incorporation of  $\text{Zr}^{4+}$  for  $\text{ZrS}_4\text{-ZIS}$ . To further explore the optimal substitution site of Zr atom, theoretical simulation is carried out to calculate the formation energy ( $E_s$ ) of defect structure. As shown in Figs. 1e and 1f, substitution of In sites by Zr atoms shows a more negative  $E_s$  ( $-1.735$  eV) than substitution of Zn sites ( $E_s = -0.982$  eV). The more negative formation energy for substitution of In sites by Zr atoms indicates that Zr is energetically in favor of substitution of In sites other than Zn sites to form a Zr–S bond. Fig. 1d presents the fitted Fourier transformed EXAFS spectra of  $\text{Zr}_{1.2}\text{-ZIS}$  and  $\text{Zr}_{4.5}\text{-ZIS}$ , and Table S2 lists the fitting parameters at the Zr K-edge. The results indicate that  $\text{Zr}_{1.2}\text{-ZIS}$  and  $\text{Zr}_{4.5}\text{-ZIS}$  maintain Zr– $\text{S}_4$  coordination similar to metal– $\text{S}_4$  coordination in the pristine  $\text{ZnIn}_2\text{S}_4$  [23] which is in good agreement with the proposed configuration in Fig. 1e.

The enlarged XRD patterns of all samples are also presented in Fig. S1b. Slight peak shifts at  $2\theta = 21.6^\circ$  to higher angles can be observed in  $\text{ZrS}_4\text{-ZIS}$  with increasing amount of  $\text{Zr}^{4+}$ , due to the lattice distortion and deformation after successful substitution of In with Zr atoms. [23] In the Raman spectra (Fig. S1d), the four peaks at  $250$ ,  $301$ ,  $346$  and  $370$   $\text{cm}^{-1}$  are attributed to  $\text{LO}_1$ ,  $\text{TO}_2$ ,  $\text{LO}_2$  (longitudinal optical mode, transverse optical mode, longitudinal optical mode) and  $\text{A}_1\text{g}$  four mode of crystal  $\text{ZnIn}_2\text{S}_4$ , respectively. [23] With the increase of  $\text{Zr}^{4+}$  amount, the intensities of all Raman peaks decrease gradually, owing to the decrease of crystalline symmetry. [37] No obvious impurity peaks of Raman spectra are observed in  $\text{ZrS}_4\text{-ZIS}$ , indicating high purity of the three materials, which is consistent with the XRD results (Fig. S1a and S1b). External atoms doping through substitution or inserting lattice interstitial would decrease the crystallinity of materials. [37] In this case, the Zr atoms enter into crystalline lattice of  $\text{ZnIn}_2\text{S}_4$  after substitution of the In sites for  $\text{ZrS}_4\text{-ZIS}$ . Although the  $\text{Zr}^{4+}$  doping content for  $\text{Zr}_{1.2}\text{-ZIS}$  is relatively low, the crystalline symmetry of  $\text{Zr}_{1.2}\text{-ZIS}$  is also slightly decreased owing to the partial mismatch of  $\text{Zr}^{4+}$  and  $\text{In}^{3+}$ , thus leading to the decreased of the Raman peaks compared with ZIS.

The morphologies of ZIS and  $\text{ZrS}_4\text{-ZIS}$  are analyzed by transmission electron micrograph (TEM), scanning transmission electron microscopy (SEM), and high-angle annular dark-field (STEM-HAADF) images (Figs. 1g–1i and S3–S9). All the materials exhibit as nanosheets, and

exhibit a  $0.33$  nm crystalline interplanar spacing in the high resolution TEM (HRTEM) images (Figs. S3b, 1h, S5b and S8b), ascribed to the (100) plane of  $\text{ZnIn}_2\text{S}_4$ , and moreover, the  $120^\circ$  intersection angle well matches with its hexagonal phase (JCPDS 72–0773). [14,23] Evidently, slight deformation appears in  $\text{Zr}_{4.5}\text{-ZIS}$  compared with more regular atoms arrangement in ZIS,  $\text{Zr}_{0.4}\text{-ZIS}$  and  $\text{Zr}_{1.2}\text{-ZIS}$  (Fig. S8), indicating the introduction of  $\text{Zr}^{4+}$  leads to lattice distortion, which can be further testified by the fast Fourier transformation (FFT) (Figs. S3c, 1h, S5c and S8c). In addition, for  $\text{Zr}_{1.2}\text{-ZIS}$  (optimized catalyst confirmed in the later sections), the STEM-HAADF image shows the lattice of  $\text{Zr}_{1.2}\text{-ZIS}$  consists of hexagonal alternating In (or Zr sites of substituted In) and sulfur sites (Fig. 1i). The STEM-energy dispersive spectroscopy (EDS) mapping of manifest  $\text{Zr}_{1.2}\text{-ZIS}$  (Fig. S7) and  $\text{Zr}_{4.5}\text{-ZIS}$  (Fig. S9) is composed of S, In, Zn, and Zr with a homogeneous dispersion of Zr atoms. This is also confirmed by the high-resolution XPS spectra (Fig. S10), where the peaks at  $445.0$ ,  $452.6$ ,  $1022.3$ ,  $1045.1$ ,  $161.6$  and  $162.8$  eV are attributed to In  $3d_{5/2}$ , In  $3d_{3/2}$ , Zn  $2p_{3/2}$ , Zn  $2p_{1/2}$ , S  $2p_{3/2}$  and S  $2p_{1/2}$  respectively, consistent with the characteristic peaks of  $\text{ZnIn}_2\text{S}_4$ . [23,38–40].

### 3.2. Mechanism on photocatalytic activation of $\text{O}_2$ by $\text{ZrS}_4\text{-ZIS}$

Generally, the pollutants can be attacked and degraded by ROS, which is generated by  $\text{O}_2$  activation at CB due to the specific band structures of ZIS as discussed in the introduction. [13] It is known that the optical and electronic properties of semiconductors are highly related to their photocatalytic activity, which are characterized through light absorption and photogenerated charge separation efficiency. Fig. S11a displays the UV–vis DRS spectra on optical properties of all materials, which all possess light absorption ranges of  $350$ – $600$  nm. The absorption edge of  $\text{Zr}_{0.4}\text{-ZIS}$ ,  $\text{Zr}_{1.2}\text{-ZIS}$  and  $\text{Zr}_{4.5}\text{-ZIS}$  displayed slightly red-shift after introduction of  $\text{Zr}^{4+}$  compared with that of pristine ZIS. The band gap ( $E_g$ ) was obtained via Kubelk–Munk method (Fig. S11b), and the  $E_g$  values of ZIS,  $\text{Zr}_{0.4}\text{-ZIS}$ ,  $\text{Zr}_{1.2}\text{-ZIS}$  and  $\text{Zr}_{4.5}\text{-ZIS}$  were  $2.18$ ,  $2.17$ ,  $2.14$  and  $2.10$  eV, respectively. Furthermore, the VB–XPS spectra was used to acquire the valence band energy ( $E_{\text{VB}}$ ) (Fig. S11c), and the  $E_{\text{VB}}$  values of ZIS,  $\text{Zr}_{0.4}\text{-ZIS}$ ,  $\text{Zr}_{1.2}\text{-ZIS}$  and  $\text{Zr}_{4.5}\text{-ZIS}$  were all  $1.69$  eV. Thus, the conduction band energies ( $E_{\text{CB}}$ ) of ZIS,  $\text{Zr}_{0.4}\text{-ZIS}$ ,  $\text{Zr}_{1.2}\text{-ZIS}$  and  $\text{Zr}_{4.5}\text{-ZIS}$  were further calculated by  $E_{\text{CB}} = E_{\text{VB}} - E_g$  [41] which were  $-0.49$ ,  $-0.48$ ,  $-0.45$  and  $-0.41$  eV, respectively. Therefore, the introduction of  $\text{Zr}^{4+}$  broadened the light response range of materials due to lower CB positions, which are also demonstrated by band structure calculation.

Generally, the regulation of d-band electrons can increase the band localization, narrow the band gap and facilitate charge transfer, then conducive to improving the photocatalytic activity. [42] The



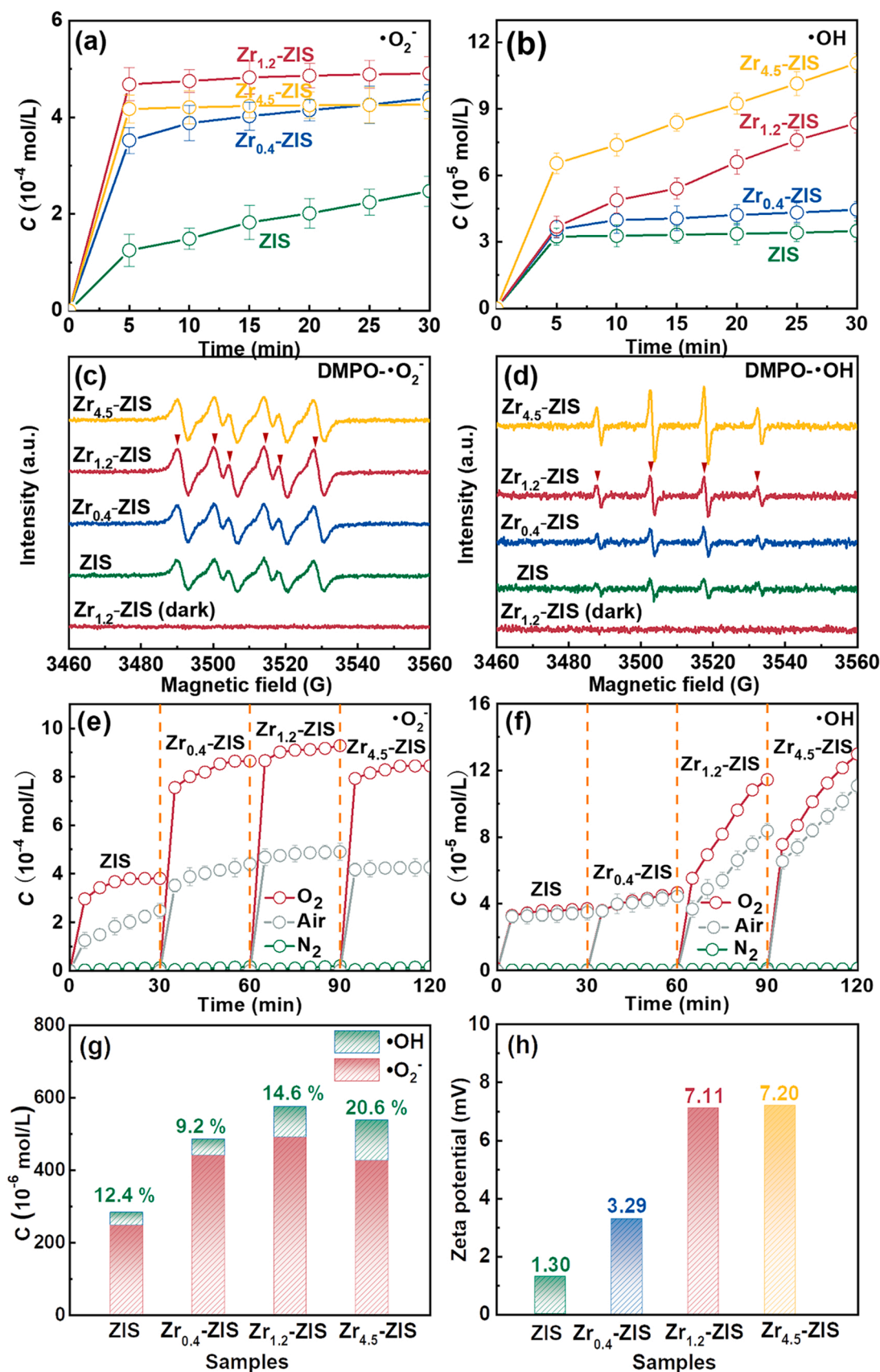


Fig. 3. Quantitative determination of (a)  $\bullet\text{O}_2^-$  and (b)  $\bullet\text{OH}$  during photocatalysis by different catalysts; ESR spectra of (c) DMPO- $\bullet\text{O}_2^-$  and (d) DMPO- $\bullet\text{OH}$  in dark and after 5 min photocatalysis; Quantitative determination of (e)  $\bullet\text{O}_2^-$  and (f)  $\bullet\text{OH}$  during photocatalysis under different gas atmospheres; (g) The proportion of  $\bullet\text{OH}$  and  $\bullet\text{O}_2^-$  in total ROS produced at 30 min for different catalysts; (h) Zeta potentials of various materials at pH 7; (Experimental conditions: Initial NBT concentration =  $2.5 \times 10^{-4}$  M, initial salicylic acid concentration = 0.2 mM, material dosage = 0.5 g/L, solution volume = 50 mL, pH =  $7.0 \pm 0.2$ ).

density-of-state (DOS) and projected density-of-state (PDOS) spectra of ZIS and  $\text{Zr}_{1.2}\text{-ZIS}$  are compared in Fig. 2. It is indicated that Zr hybridization for  $\text{Zr}_{1.2}\text{-ZIS}$  narrows the CB position, resulting in a lower conduction band minimum (CBM, 1.89 eV) compared with 1.99 eV of ZIS. Moreover, although the conduction band maximum (VBM) does not change for  $\text{Zr}_{1.2}\text{-ZIS}$  (0.29 eV) compared with ZIS, the primary VB peak centered at  $-0.26$  eV for ZIS splits into three peaks ( $-0.05$ ,  $-0.31$  and  $-0.53$  eV) for  $\text{Zr}_{1.2}\text{-ZIS}$ , indicating enhanced delocalization of valence electrons contributed by D-band electrons,[42] which have higher mobility to be excited to CB. The PDOS spectra also indicate that the introduced Zr in  $\text{Zr}_{1.2}\text{-ZIS}$  mainly contributes the CB, which can provide unoccupied orbital to accept excited photo-electron,[42] in favor of subsequent oxygen activation and photocatalytic degradation of TC. Evidently, the photogenerated electrons ( $e^-$ ) in CB of all the catalysts can react with  $\text{O}_2$  to produce  $\bullet\text{O}_2^-$  ( $E(\text{O}_2/\bullet\text{O}_2^-) = -0.33$  eV vs. NHE) due to more negative CB positions (Fig.S11d). However, the photogenerated holes ( $h^+$ ) in VB of the materials (1.69 eV vs. NHE) cannot oxidize  $\text{H}_2\text{O}$  ( $E(\bullet\text{OH}/\text{H}_2\text{O}) = 2.38$  eV vs. NHE) or  $\text{OH}^-$  ( $E(\bullet\text{OH}/\text{OH}^-) = 2.72$  eV vs. NHE) to  $\bullet\text{OH}$  due to lower VB energies (Fig.S11d). Therefore, activation of  $\text{O}_2$  to  $\bullet\text{O}_2^-$  at VB is focused and the mechanism is further revealed.

The photogenerated charge carrier separation, transfer and recombination of the catalysts are further analyzed by EIS, transient photocurrent and PL spectra. Fig.S12a shows  $\text{Zr}_{1.2}\text{-ZIS}$  had the smallest arc radius and lowest charge transfer resistance ( $R_t$ ) of 2.8 k $\Omega$  among all the catalysts. Similarly, the transient photocurrent density in Fig.S12b displays  $\text{Zr}_{1.2}\text{-ZIS}$  exhibited the highest current density, which was about 4.1, 1.7 and 1.8 times as that of ZIS,  $\text{Zr}_{0.4}\text{-ZIS}$  and  $\text{Zr}_{4.5}\text{-ZIS}$ , respectively. All the results above confirmed the best separation and transfer of photogenerated electron-hole pairs of  $\text{Zr}_{1.2}\text{-ZIS}$ . In addition, PL spectra in Fig.S13 shows  $\text{Zr}_{1.2}\text{-ZIS}$  also exhibited lowest PL peak intensity, indicating the lowest recombination rate of photogenerated charge carrier for  $\text{Zr}_{1.2}\text{-ZIS}$ .

The better separation/transfer efficiency and lower recombination rate of photogenerated charge carrier of  $\text{Zr}_{1.2}\text{-ZIS}$  facilitate  $\text{O}_2$  activation to ROS. The photocatalytic  $\text{O}_2$  activation process and mechanism are then investigated by the ROS quantitative determination, ESR spectra, and DFT calculations. Fig. 3a indicates that the highest concentration of  $\bullet\text{O}_2^-$  (490.9  $\mu\text{mol/L}$ ) was generated over  $\text{Zr}_{1.2}\text{-ZIS}$  in 30 min compared with that of ZIS (247.4  $\mu\text{mol/L}$ ),  $\text{Zr}_{0.4}\text{-ZIS}$  (439.9  $\mu\text{mol/L}$ ) and  $\text{Zr}_{4.5}\text{-ZIS}$  (426.3  $\mu\text{mol/L}$ ). Thus,  $\text{Zr}_{1.2}\text{-ZIS}$  exhibited high ability of  $\text{O}_2$  activation, which was further confirmed by ESR analysis. Fig. 3c displays a typical DMPO- $\bullet\text{O}_2^-$  adduct characteristic six-line ESR signal (characteristic spectrum parameters of  $A_N = 14$  G and  $A_H = 10$  G) for all samples after 5 min light irradiation, indicating production of  $\bullet\text{O}_2^-$  during photocatalysis.[43] However, the production of  $\bullet\text{OH}$  was different (Fig. 3b), as the  $\bullet\text{OH}$  yield gradually enhanced with increasing Zr<sup>4+</sup> amount. At 30 min, the  $\bullet\text{OH}$  concentration was 34.9, 44.5, 83.7 and 110.7  $\mu\text{mol/L}$  for ZIS,  $\text{Zr}_{0.4}\text{-ZIS}$ ,  $\text{Zr}_{1.2}\text{-ZIS}$  and  $\text{Zr}_{4.5}\text{-ZIS}$ , respectively. Similar trend was also found in ESR spectra (Fig. 3d), as the characteristic DMPO- $\bullet\text{OH}$  adduct signal with relative intensity of 1:2:2:1 was identified for all the catalysts after 5 min irradiation.[43] In addition, the intensity of DMPO- $\bullet\text{OH}$  signal gradually increased with the increase of Zr<sup>4+</sup> amount. Therefore, it is interesting that the generation of  $\bullet\text{O}_2^-$  and  $\bullet\text{OH}$  was different on the  $\text{ZrS}_4\text{-ZIS}$  materials. Although  $\bullet\text{O}_2^-$  was the primary ROS in all material systems,  $\text{Zr}_{1.2}\text{-ZIS}$  had the highest  $\bullet\text{O}_2^-$  production efficiency while  $\text{Zr}_{4.5}\text{-ZIS}$  exhibited the highest  $\bullet\text{OH}$  yield (Fig. 3g). As a result, modification of ZIS by different amounts of Zr<sup>4+</sup> achieves different pathways for ROS production, and the mechanism will be discussed in details later based on DFT calculations. It is worth noting that the holes ( $h^+$ ) of all the ZIS catalysts in this study cannot achieve oxidation of  $\text{H}_2\text{O}/\text{OH}^-$  to  $\bullet\text{OH}$  according to their low VB energies (Fig. S11d), so  $\bullet\text{OH}$  is formed at the CB according to Eqs. 5–8:[44,45].

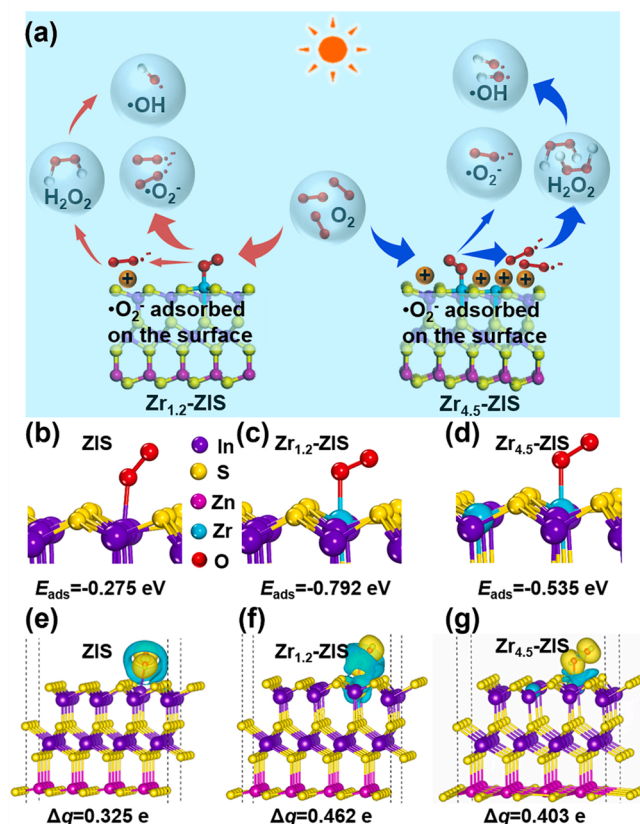
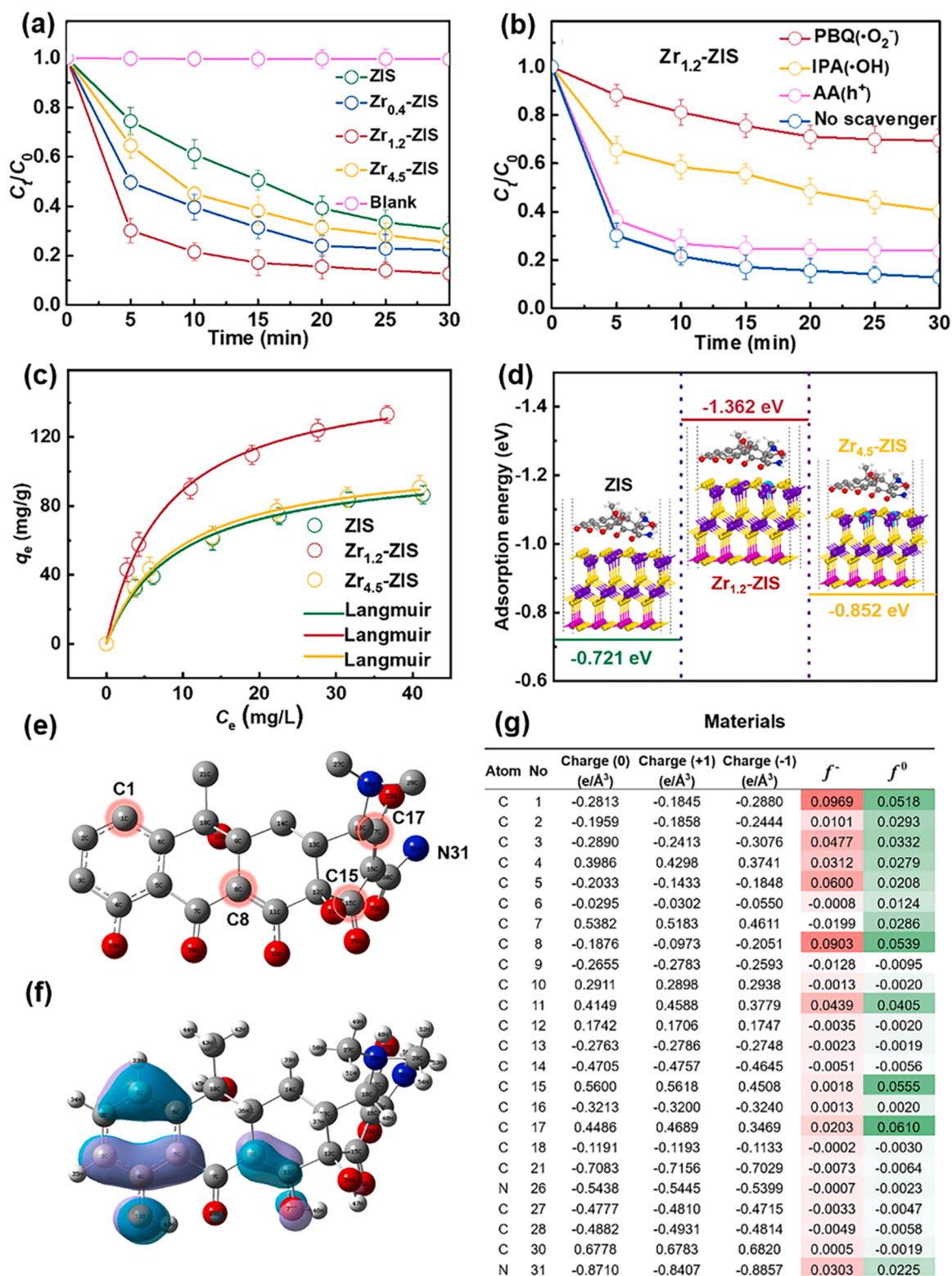


Fig. 4. (a) The mechanism of  $\bullet\text{O}_2^-$  and  $\bullet\text{OH}$  formation at the surface of materials; The adsorption energies of  $\text{O}_2$  on (b) ZIS, (c)  $\text{Zr}_{1.2}\text{-ZIS}$  and (d)  $\text{Zr}_{4.5}\text{-ZIS}$ ; The electron transfer from (e) ZIS, (f)  $\text{Zr}_{1.2}\text{-ZIS}$  and (g)  $\text{Zr}_{4.5}\text{-ZIS}$  to  $\text{O}_2$  (yellow area is the electron accumulation area and blue area is the electron dissipation area).



To further clarify the source and formation pathway of ROS, quantitation of  $\bullet\text{O}_2^-$  and  $\bullet\text{OH}$  were conducted in different atmospheres including nitrogen ( $\text{DO} < 0.10$  mg/L), air ( $\text{DO} = 7.14$  mg/L) and oxygen ( $\text{DO} = 16.15$  mg/L), respectively. Apparently, the production of  $\bullet\text{O}_2^-$  was significantly improved in oxygen atmosphere while could not occur in nitrogen for all materials (Fig. 3e), verifying  $\bullet\text{O}_2^-$  originated from  $\text{O}_2$ . Similarly, the  $\bullet\text{OH}$  concentration was further enhanced in oxygen atmosphere while was ignorable in nitrogen (Fig. 3f), suggesting  $\bullet\text{OH}$  also originated from  $\text{O}_2$ , consistent with the  $\text{O}_2 \rightarrow \bullet\text{O}_2^- \rightarrow \text{H}_2\text{O}_2 \rightarrow \bullet\text{OH}$  multi-step one-electron reduction pathway. Noticeably, the generation ability of  $\bullet\text{OH}$  over the samples was different from that of  $\bullet\text{O}_2^-$ . It is because  $\text{Zr}_{4.5}\text{-ZIS}$  exhibited the highest zeta potential (7.20 eV) at pH 7 (Fig. 3h), and the electropositive surface was beneficial to adsorb the negatively charged  $\bullet\text{O}_2^-$ , leading to further reduction reaction of  $\bullet\text{O}_2^-$  to  $\text{H}_2\text{O}_2$  and finally  $\bullet\text{OH}$ , which can be further confirmed by DFT calculation in Fig. S14. The adsorption energies ( $E_{\text{ads}}$ ) of  $\bullet\text{O}_2^-$  on ZIS,  $\text{Zr}_{1.2}\text{-ZIS}$  and  $\text{Zr}_{4.5}\text{-ZIS}$  are 0.191,  $-1.246$  and  $-1.321$  eV, respectively. The adsorption energy of  $\bullet\text{O}_2^-$  for catalysts becomes more negative with the increase of Zr dosage, indicating gradually enhanced adsorption capacity of  $\bullet\text{O}_2^-$  with the increase of Zr dosage, resulting in more  $\bullet\text{O}_2^-$  to be converted into  $\text{H}_2\text{O}_2$  and finally  $\bullet\text{OH}$ .

The mechanism on activation of  $\text{O}_2$  for production of  $\bullet\text{O}_2^-$  and  $\bullet\text{OH}$  at the interface of  $\text{Zr}_{1.2}\text{-ZIS}$  and  $\text{Zr}_{4.5}\text{-ZIS}$  is illustrated in Fig. 3a.  $\text{Zr}_{4.5}\text{-ZIS}$  with higher zeta potential exhibits stronger surface charge effect, which promotes the adsorption capacity of  $\bullet\text{O}_2^-$ , thus facilitating the reduction



**Fig. 5.** (a) Photocatalytic degradation of TC by various materials; (b) Photocatalytic degradation of TC by  $Zr_{1.2}$ -ZIS in the presence of different scavengers; (c) Adsorption isotherms and (d) adsorption energies of TC by ZIS,  $Zr_{1.2}$ -ZIS and  $Zr_{4.5}$ -ZIS; DFT calculations on TC molecule at the B3LYP/6-31 + g(d,p) level; (e) Chemical structure; (f) HOMO distributions; (g) Natural population analysis (NPA) charges and calculated Fukui index ( $f^-$  and  $f^0$ ). (For photocatalysis tests: initial TC concentration = 20 mg/L, material dosage = 0.5 g/L, solution volume = 50 mL, pH = 7.0 ± 0.2; scavenger dosage = 0.5 mM for Fig. 5 f. For adsorption isotherms tests, initial TC concentration = 0–200 mg/L, material dosage = 0.5 g/L, pH = 7.0 ± 0.2, solution volume = 40 mL, temperature = 25 °C and equilibrium time = 24 h).



of  $\bullet\text{O}_2$  for generation of  $\text{H}_2\text{O}_2$  and  $\bullet\text{OH}$ . The proportion of produced  $\bullet\text{OH}$  in total ROS for ZIS,  $\text{Zr}_{0.4}\text{-ZIS}$ ,  $\text{Zr}_{1.2}\text{-ZIS}$  and  $\text{Zr}_{4.5}\text{-ZIS}$  are 12.4%, 9.2%, 14.6% and 20.6%, respectively (Fig. 3g). It can be noted that the proportion of  $\bullet\text{OH}$  in total ROS for  $\text{Zr}_{0.4}\text{-ZIS}$  is not consistent tendency of  $\bullet\text{OH}$  yield (Fig. 3b), which can be possibly attributed to unobtrusive surface charge effect. In the process of activation of  $\text{O}_2$  for  $\text{Zr}_{0.4}\text{-ZIS}$ , the generation of  $\bullet\text{O}_2$  (439.9  $\mu\text{mol/L}$ ) derived from  $\text{O}_2$  was significantly improved compared with ZIS (247.4  $\mu\text{mol/L}$ ). Nevertheless, due to unobtrusive surface charge effect of  $\text{Zr}_{0.4}\text{-ZIS}$ , the adsorption capacity of  $\bullet\text{O}_2$  (final conversion to  $\bullet\text{OH}$ ) of  $\text{Zr}_{0.4}\text{-ZIS}$  did not increase exponentially, resulting in improved  $\bullet\text{OH}$  concentration and lower proportion of  $\bullet\text{OH}$  in total ROS compared with ZIS. For the generation of  $\bullet\text{O}_2$ ,  $\text{Zr}_{1.2}\text{-ZIS}$  had the best  $\text{O}_2$  activation ability, which was further explored by DFT calculation. The adsorption energies ( $E_{\text{ads}}$ ) of  $\text{O}_2$  on ZIS,  $\text{Zr}_{1.2}\text{-ZIS}$  and  $\text{Zr}_{4.5}\text{-ZIS}$  are  $-0.275$ ,  $-0.792$  and  $-0.535$  eV, respectively (Fig. 4b-d). Therefore, the most negative adsorption energy of  $\text{Zr}_{1.2}\text{-ZIS}$  suggests best  $\text{O}_2$  adsorption capability, thus promoting the subsequent  $\text{O}_2$  activation. In addition, the charge density difference calculation results (Fig. 4e-g) reveal  $\text{Zr}_{1.2}\text{-ZIS}$  possess more electron transfer of 0.462 e into  $\text{O}_2$ , higher than 0.325 e of ZIS and 0.403 e of  $\text{Zr}_{4.5}\text{-ZIS}$ , further corroborating better  $\text{O}_2$  activation ability of  $\text{Zr}_{1.2}\text{-ZIS}$ .

### 3.3. Photocatalytic degradation of TC and contributions of ROS in different catalysts systems

In order to explore the photocatalytic activity of the catalysts, the optical parameters were first studied. The extinction coefficient was calculated according to the Beer-Lambert law[46]:

$$A = -\lg(I/I_0) = \epsilon bc \quad (9)$$

in which  $A$ ,  $I$ ,  $I_0$ ,  $\epsilon$ ,  $b$ ,  $c$  are absorbance, transmitted light intensity, incident light intensity, extinction coefficient, optical path length and concentration of light-absorbing substance, respectively.

The average extinction coefficients can be acquired through the average absorbance in Table S3. It can be observed that all catalysts have similar absorbance about 1, indicating the structure of  $\text{ZrS}_4\text{-ZIS}$  is similar to ZIS and still maintains a nanosheet structure according to the results of TEM in Fig. 1g, S3a, S5a and S8a. In addition, the average extinction coefficients are similar, indicating all catalysts possess similar light absorption ability. The reactor geometry was acquired by formula[47,48]:

$$\alpha = H/L \quad (10)$$

$$\beta = L/\eta R \quad (11)$$

in which  $H$ ,  $L$ ,  $\eta$  and  $R$  are length of the reactor, lamp length, ratio of internal radius to external radius of annulus and external radius of annulus, respectively.

$A$  and  $\beta$  are 1.2 and 4.35. The Optical thickness ( $\tau$ ) of catalysts is significantly related to photon absorption efficiency. And the optimal range of  $\tau$  was 1.8–4.4 according to the previous reports[46,48]. The  $\tau$  of aqueous suspension can be evaluated by formula[46]:

$$\tau = hC\epsilon \quad (12)$$

in which  $h$ ,  $C$  and  $\epsilon$  are depth of liquid in the reactor, catalyst concentration and average extinction coefficient, respectively.

As shown in Table S4, the optical thickness of all catalysts has an approximate positive coefficient linear relationship with catalyst dosage. In Fig. S15, when the material dosage of all catalysts is 0.5 g/L, the ZIS,  $\text{Zr}_{0.4}\text{-ZIS}$ ,  $\text{Zr}_{1.2}\text{-ZIS}$  and  $\text{Zr}_{4.5}\text{-ZIS}$  exhibit optimal photocatalytic degradation activity of 69.4%, 77.8%, 87.3% and 74.7% for TC compared with other material dosage under the same conditions. The suitable optical thickness of ZIS,  $\text{Zr}_{0.4}\text{-ZIS}$ ,  $\text{Zr}_{1.2}\text{-ZIS}$  and  $\text{Zr}_{4.5}\text{-ZIS}$  (0.5 g/L) are all 3. Therefore, the optical thickness (3) of all catalysts (0.5 g/L) can be determined as the best value used in the photocatalytic experiment.

Moreover, the effective utilization of photons is an important factor affecting the photocatalytic performance. The quantum yield of fluorescence (QY) measurement was tested for reflecting the total rate of photon absorption[46]. As shown in Fig. S16, the  $\text{Zr}_{1.2}\text{-ZIS}$  possesses larger QY (1.43%) than that of ZIS (0.17%),  $\text{Zr}_{0.4}\text{-ZIS}$  (1.06%) and  $\text{Zr}_{4.5}\text{-ZIS}$  (0.96%), suggesting its higher utilization rate of light energy, in accordance with higher photocatalytic activity of  $\text{Zr}_{1.2}\text{-ZIS}$ . In order to better study the adsorption and degradation performance of TC, the speciation of TC was first studied. As shown in Fig. S17, the  $\text{pK}_a$  values of amphoteric molecule TC are 3.3, 7.7, 9.7 and 12.0. It predominantly exists as positively, neutral and negatively charged at pH 3, 7, and 9, respectively. Consequently, the speciation of TC is mainly neutral charged at  $\text{pH } 7.0 \pm 0.2$ . [49,50]. Fig. 5a presents the degradation of TC by various catalysts (0.5 g/L) under visible light irradiation, and the presented TC removal was all attributed to degradation after NaOH extraction (described in Section 2.2).  $\text{Zr}_{1.2}\text{-ZIS}$  showed the highest photocatalytic activity, as 87.3% of TC was degraded with a 37.9% mineralization rate (TOC removal) in 30 min, which was higher than the TC degradation efficiency of ZIS (69.4%),  $\text{Zr}_{0.4}\text{-ZIS}$  (77.8%) and  $\text{Zr}_{4.5}\text{-ZIS}$  (74.7%). In addition, Fig.S18a shows  $\text{Zr}_{1.2}\text{-ZIS}$  had the highest rate constant value ( $k_1$ ) of  $0.145 \text{ min}^{-1}$  for TC degradation. Fig.S18c displays only 0.006% of In and 0.234% of Zn were dissolved for  $\text{Zr}_{1.2}\text{-ZIS}$  after reaction, respectively. Fig.S18d indicates 80.8% of TC also could be degraded at 30 min for  $\text{Zr}_{1.2}\text{-ZIS}$  after five cycles. The above results indicated good stability and reusability of  $\text{Zr}_{1.2}\text{-ZIS}$ . Furthermore, scavenger quenching tests indicate the contribution of reactive species to TC degradation was ranked as  $\bullet\text{O}_2 > \bullet\text{OH} > \text{h}^+$  (Fig. 5b). Then, based on the  $k_1$  values of TC degradation in the presence of different scavengers listed in Fig.S18b, the contributions of specific reactive species were calculated by Eqs. 2–4, which was 87.1% of  $\bullet\text{O}_2$ , 71.1% of  $\bullet\text{OH}$  and 20.9% of  $\text{h}^+$ , respectively. The both high  $\bullet\text{O}_2$  and  $\bullet\text{OH}$  contribution rates also indicated  $\bullet\text{OH}$  was derived from  $\bullet\text{O}_2$ . Similarly, Fig.S19 indicates  $\bullet\text{O}_2$  also played the dominant roles in the systems using other three materials (82.1%, 86.9% and 85.0% respectively). Meanwhile, the contribution of  $\bullet\text{OH}$  increased from 46.7% for ZIS to 73.7% for  $\text{Zr}_{4.5}\text{-ZIS}$  with the increasing Zr amount, which is in good agreement with the radical yield results (Figs. 3b and 3f). Therefore,  $\bullet\text{O}_2$  plays the most important role in the photocatalysis systems using ZIS and  $\text{ZrS}_4\text{-ZIS}$ : 1)  $\bullet\text{O}_2$  can directly oxidize TC for degradation, and 2)  $\bullet\text{O}_2$  can transform into  $\bullet\text{OH}$  for electrophilic attack.  $\bullet\text{O}_2$  accounts for the formation of  $\bullet\text{OH}$ , so quenching of  $\bullet\text{O}_2$  also leads to no production of  $\bullet\text{OH}$ .

Generally, the heterogeneous photocatalytic reaction for pollutant degradation contains two processes: 1) production of reactive species, and 2) adsorption of target pollutant on the surface of catalyst and then attack by reactive species.[51–53] The quantitation of ROS shown in Fig. 3h has confirmed  $\text{Zr}_{1.2}\text{-ZIS}$  had the highest total ROS yield (574.6  $\mu\text{mol/L}$  at 30 min). Meanwhile, DFT calculations in Fig. 4 have demonstrated the highest adsorption ability of  $\text{O}_2$  by  $\text{Zr}_{1.2}\text{-ZIS}$ . However, it is worth noting that the total ROS of  $\text{Zr}_{1.2}\text{-ZIS}$  (574.6  $\mu\text{mol/L}$ ) and  $\text{Zr}_{4.5}\text{-ZIS}$  (537.0  $\mu\text{mol/L}$ ) are close (Fig. 3h), which is not consistent with the big difference in photocatalytic performance (Fig. 5a). Therefore, the adsorption of TC on the surface of catalyst is also important, which is further studied through adsorption isotherm experiments (Text S7 and Fig. 5c) and DFT calculation (Fig. 5d). Table S5 lists the simulated parameters of Langmuir and Freundlich isotherm models. The high correlation coefficients ( $R^2 > 0.99$ ) of Langmuir model for all materials indicated TC preferred a monolayer adsorption on the catalysts[51]. In addition,  $\text{Zr}_{1.2}\text{-ZIS}$  has the largest monolayer maximum adsorption capacity ( $q_m = 158.3 \text{ mg/g}$ ) of TC, which is much higher than that of  $\text{Zr}_{4.5}\text{-ZIS}$  ( $q_m = 109.3 \text{ mg/g}$ ), in agreement with the better TC degradation efficiency (Fig. 5a). Moreover, Fig. 5d indicates  $\text{Zr}_{1.2}\text{-ZIS}$  shows the most negative adsorption energy ( $-1.362 \text{ eV}$ ) for TC compared with ZIS ( $-0.721 \text{ eV}$ ) and  $\text{Zr}_{4.5}\text{-ZIS}$  ( $-0.852 \text{ eV}$ ), demonstrating  $\text{Zr}_{1.2}\text{-ZIS}$  has the strong adsorption affinity to TC, thus facilitating TC photocatalytic degradation.

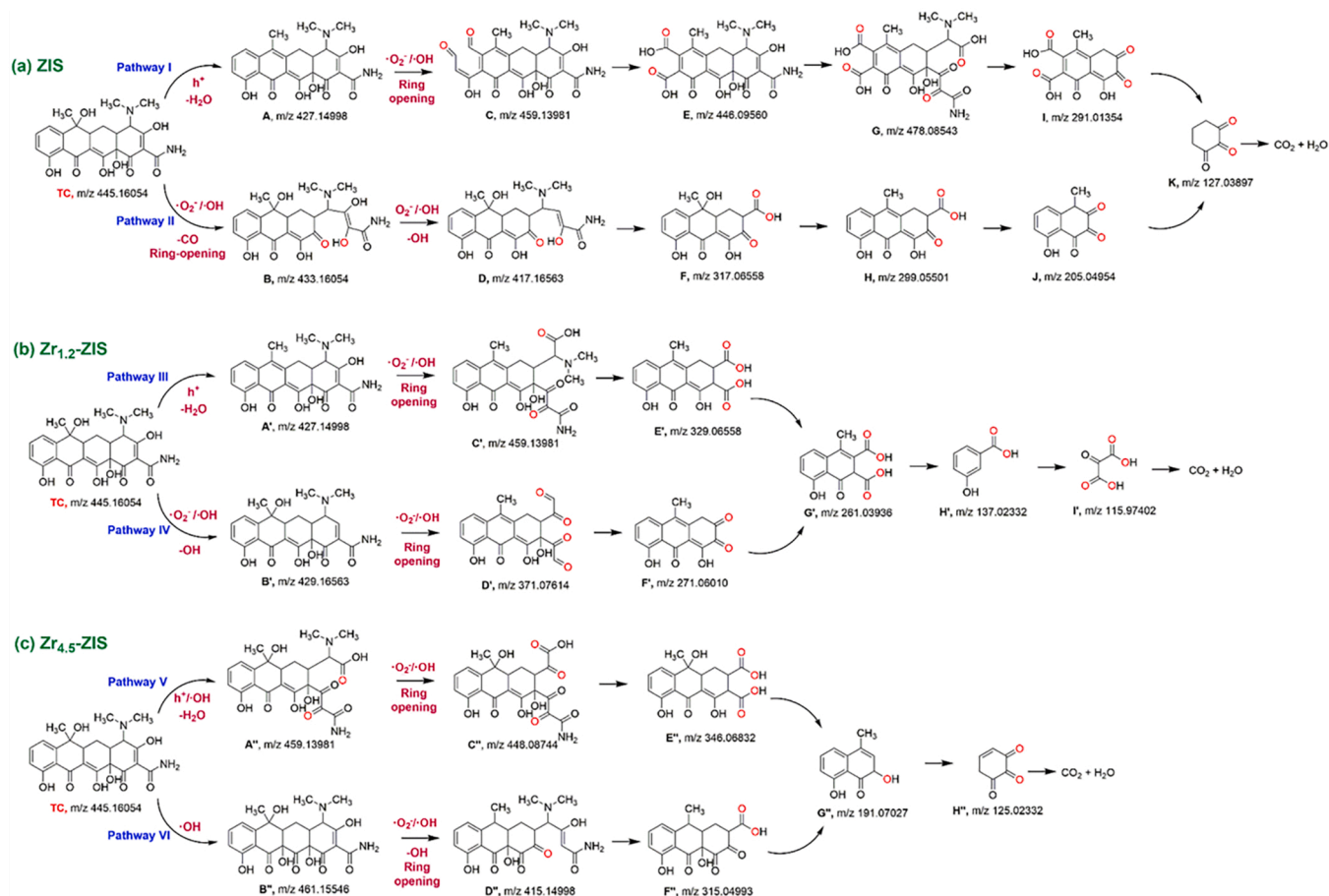


Fig. 6. Proposed photocatalytic degradation pathways of TC over (a) ZIS, (b)  $Zr_{1.2}$ -ZIS and (c)  $Zr_{4.5}$ -ZIS.

### 3.4. DFT calculations on reactive sites of TC and its degradation pathways

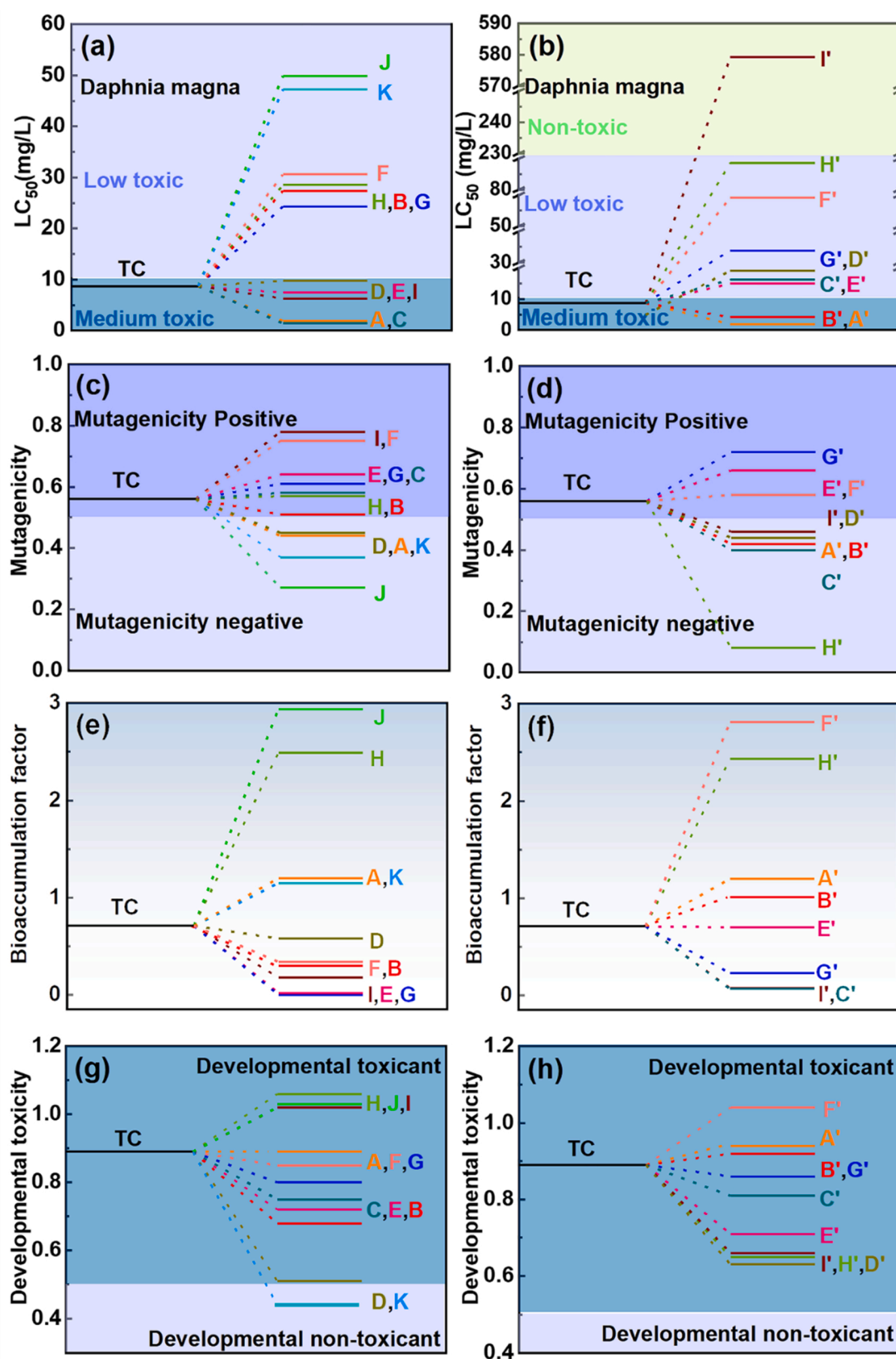
The photocatalytic degradation intermediates/products of TC by ZIS,  $Zr_{1.2}$ -ZIS and  $Zr_{4.5}$ -ZIS are identified separately by UHPLC-MS (Orbitrap). Tables S6–S8 present the chemical structures,  $m/z$ , and retention times of TPs based on mass spectrum analysis. It is interesting that most of TPs were different for the photocatalysis systems of ZIS,  $Zr_{1.2}$ -ZIS and  $Zr_{4.5}$ -ZIS. DFT calculation on Fukui index is introduced to evaluate the reactive sites of TC (Figs. 5e–5g). Fig. 5f displays the highest occupied molecular orbital (HOMO) of TC, which mainly locates on the benzene ring, C8 and C11 atoms. HOMO represents the regions that can easily lose electron and prefer to be oxidized by reactive species, while it can precisely and quantitatively describe the reactive sites.[54] Therefore, Fukui index is calculated to present the regioselectivity of different atoms of TC (Fig. 5g). In this study,  $\bullet O_2$  and  $\bullet OH$  are the dominant ROS, which can be recognized as electrophilic or radical attacks.[32] For TC molecule, the most reactive sites for electrophilic attack ( $f^-$ ) are C1 ( $f^- = 0.0969$ ) and C8 ( $f^- = 0.0903$ ); while for radical attack ( $f^0$ ) are C1 ( $f^0 = 0.0518$ ), C8 ( $f^0 = 0.0539$ ), C15 ( $f^0 = 0.0555$ ) and C17 ( $f^0 = 0.0610$ ) (Fig. 5g). Higher  $f^-$  or  $f^0$  value indicates the higher reactivity of the site for the attack by  $\bullet O_2$  and  $\bullet OH$ .

Fig. 6 presents the degradation pathways of TC by using different materials. For ZIS (Fig. 6a), a dehydrated product TP A was identified after hole attack (Pathway I), which was further oxidized to TP C after benzene ring opening at the reactive site of C1 ( $f^- = 0.0969$  and  $f^0 = 0.0518$ ). Meanwhile, radicals attack on the reactive site of C15 with high  $f^0$  value led to the formation of TP B via a ring opening reaction (Pathway II). A series of radical-addition, dehydration, and decarboxylation reactions occurred, leading to deep oxidation and mineralization

of TPs. For  $Zr_{1.2}$ -ZIS (Fig. 6b), TP A' was acquired via dehydration by hole oxidation (Pathway III), while radicals attacking on the C17 site with the highest  $f^0$  value (0.0610) led to dihydroxylation for formation of B' (Pathway IV), and further ring opening for formation of TPs D' and C' (from A') via the dehydroxylation. Moreover, deep oxidation by resulted in the formation of small molecule products such as 3-hydroxybenzoic acid (H') and 2-oxomalonic acid (I'), and even mineralization products of  $CO_2$  and  $H_2O$ . For  $Zr_{4.5}$ -ZIS (Fig. 6c), high yield of  $\bullet OH$  was obtained in this system (Figs. 3b and 3h), which preferred to attack the C17 and C8 sites with high Fukui values. As a result, TP A'' through ring opening reaction and TP B'' through hydroxylation ( $\bullet OH$  addition) were produced at the initial stage. Afterwards, further dealkylation, decarboxylation and demethylation occurred, then deep oxidation product cyclohex-4-ene-1,2,3-trione (H'') was formed and finally mineralized. The different identified degradation pathways indicated that the proportion of  $\bullet O_2/\bullet OH$  in photocatalysis system can affect the transformation of organic pollutant, so regulation of the Zr amount in  $ZrS_4$ -ZIS achieved successful control of ROS production and TC transformation.

### 3.5. Ecotoxicity evaluation on degradation intermediates of TC in different catalysts systems

The toxicity of TP is an important factor in evaluating its environmental safety and potential risk. To examine the ecotoxicity of TC and its TPs, four toxicity indexes, i.e. *Daphnia magna* LC<sub>50</sub> (48 h), mutagenicity, bioaccumulation factor and developmental toxicity, were calculated using Toxicity Estimation Software Tool (T.E.S.T., Version 5.1.1) by quantitative structure-activity relationships (QSARs) methodologies from United States Environmental Protection Agency (EPA) database.



**Fig. 7.** Toxicity evaluation: (a) *Daphnia magna*  $LC_{50}$  (48 h), (c) mutagenicity, (e) bioaccumulation factor and (g) development toxicity of TC and its degradation intermediates for Zr<sub>1.2</sub>-ZIS; (b) *Daphnia magna*  $LC_{50}$  (48 h), (d) mutagenicity, (f) bioaccumulation factor and (h) development toxicity of TC and its degradation intermediates for Zr<sub>1.2</sub>-ZIS.



[32,55].

For the parent TC, the *Daphnia magna* LC<sub>50</sub> (48 h) and mutagenicity values are 8.70 mg/L and 0.56, which represent “medium toxic” and positive result, respectively (Fig. 7a). In addition, TC is recognized a toxicant due to its high bioaccumulation factor (0.71) and development toxicity (0.89), respectively. Generally, the TPs identified in the photocatalysis system using Zr<sub>1.2</sub>-ZIS exhibit lower ecotoxicities than that using ZIS. The deep oxidation products, i.e. TPs H' and I' in Zr<sub>1.2</sub>-ZIS system while J and K in ZIS system, are focused as they represent the transformation products at the final stage of photocatalytic reaction. Specifically, for *Daphnia magna* LC<sub>50</sub>, Zr<sub>1.2</sub>-ZIS converts TC to deep oxidation TP of H' (LC<sub>50</sub> = 88.62 mg/L) with much lower toxicity, and even non-toxic product of I' (LC<sub>50</sub> = 579.24 mg/L) (Fig. 7b); however, the deep oxidation TPs (e.g., J with LC<sub>50</sub> of 49.91 mg/L and K of 47.25 mg/L) by using ZIS exhibit higher toxicity due to low LC<sub>50</sub> values (Fig. 7a). For mutagenicity, most of TPs (A', B', C', D', H' and I') in Zr<sub>1.2</sub>-ZIS system reveal mutagenicity negative (Fig. 7d), while most of TPs (B, C, E, F, G, H and I) in ZIS system show positive results (Fig. 7c). For bioaccumulation, deep oxidation product I' has low bioaccumulation factor of 0.075 for Zr<sub>1.2</sub>-ZIS (Fig. 7f), while both J (2.94) and H (2.49) show high bioaccumulation factors for ZIS (Fig. 7e). For development toxicity, H' (0.65) and I' (0.66) in Zr<sub>1.2</sub>-ZIS system have lower toxicity than J (0.96) in ZIS system (Figs. 7g and 7h). Therefore, Zr<sub>1.2</sub>-ZIS after Zr-S<sub>4</sub> active sites regulation not only exhibit high photocatalytic activity for TC degradation, but also converts TC to lower toxicity TPs owing to the specific species and proportion of produced ROS.

In the photocatalysis system of Zr<sub>1.2</sub>-ZIS, TPs A', B', C', D', and E' were formed through dehydration, dehydroxylation and ring-opening processes in the initial stage, and the toxicity indexes of these TPs are not significantly decrease except for the mutagenicity of A', B' and C', due to the potential low hydrophilicity of these TPs. After deeper oxidation, the newly formed TPs generally present lower ecotoxicities. However, TP F' shows higher bioaccumulation factor (2.81) (Fig. 7) and development toxicity (1.04) (Fig. 7h) than parent TC and other TPs due to higher hydrophilicity via the abstraction of hydrophilic groups and ring-opening process. Overall, the toxicity evaluation suggested the developed photocatalysis method using Zr<sub>1.2</sub>-ZIS can significantly reduce the toxicity of TC, which is a green and environmentally friendly technology. However, it is worth noting that deep oxidation or even mineralization are necessary to greatly eliminate the toxicity of TPs.

#### 4. Conclusion

In this work, highly positive charged Zr-S<sub>4</sub> active sites are successfully constructed on the surface of ZnIn<sub>2</sub>S<sub>4</sub> nanosheets (ZrS<sub>4</sub>-ZIS) through a simple hydrothermal method. Experimental and DFT calculation results demonstrate Zr<sub>1.2</sub>-ZIS exhibited better O<sub>2</sub> activation ability than ZIS, Zr<sub>0.4</sub>-ZIS and Zr<sub>4.5</sub>-ZIS. Zr<sub>1.2</sub>-ZIS exhibited more negative O<sub>2</sub> adsorption energy, higher electron transfer efficiency into O<sub>2</sub> and better charge separation/transfer and lower recombination rate of photo-generated charge carriers in the photocatalytic process, thus leading to higher •O<sub>2</sub> yield after O<sub>2</sub> activation. In addition, Zr<sub>1.2</sub>-ZIS and Zr<sub>4.5</sub>-ZIS exhibited higher conversion efficiency of •OH evolved from O<sub>2</sub> than ZIS, and it is because their higher electropositivity promoted the adsorption of negative •O<sub>2</sub> on the surface of materials, thus facilitating further reduction reaction of •O<sub>2</sub> into H<sub>2</sub>O<sub>2</sub> and finally •OH. Photocatalysis experiments indicated Zr<sub>1.2</sub>-ZIS had the highest photocatalytic activity for TC degradation, mainly due to the high O<sub>2</sub> activation ability and large adsorption capacity of TC. Furthermore, different transformation products and degradation pathways of TC were found for ZIS, Zr<sub>1.2</sub>-ZIS and Zr<sub>4.5</sub>-ZIS, and it is highly related to the different species and proportions of ROS produced by materials after Zr-S<sub>4</sub> regulation. The degradation for TC by using Zr<sub>1.2</sub>-ZIS mainly proceeded as removal of H<sub>2</sub>O and -OH in the initial stage, and subsequent ring opening reaction dealkylation, and decarboxylation in the deep oxidation stage. It is important that significant toxicity attenuation of TPs in the TC

degradation by Zr<sub>1.2</sub>-ZIS was found, suggesting its great application potential in practical water treatment area.

#### CRedit authorship contribution statement

**Hui Li:** Investigation, Formal analysis, Writing - original draft. **Haodong Ji:** Investigation, Formal analysis, Software. **Jiajia Liu:** Investigation, Formal analysis. **Wen Liu:** Investigation, Formal analysis, Methodology, Supervision. **Fan Li:** Investigation, Formal analysis. **Zhurui Shen:** Conceptualization, Methodology, Supervision.

#### Declaration of Competing Interest

The authors declare that they have no known competing financial interests or personal relationships that could have appeared to influence the work reported in this paper.

#### Data availability

Data will be made available on request.

#### Acknowledgements

This work is supported by the National Natural Science Foundation of China (Nos. 21872102, 22172080, 52270053), the National Key Research and Development Program of China (No. 2021YFA1202500), the Beijing Nova Program (20220484215), Tianjin “Project + Team” Innovation Team Project and the Key Special Projects for Science and Technology of Inner Mongolia (No. 2021EEDSCXSFQZD001).

#### Appendix A. Supporting information

Supplementary data associated with this article can be found in the online version at doi:10.1016/j.apcatb.2023.122481.

#### References

- [1] L. Ma, Q. Cai, S.L. Ong, Z. Yang, W. Zhao, J. Duan, J. Hu, Photonic efficiency optimization-oriented dependence model of characteristic coupling spectrum on catalytic absorbance in photocatalytic degradation of tetracycline hydrochloride, *Chem. Eng. J.* 451 (2023), 138623.
- [2] Y. Wu, G. Feng, R. Huang, B. Liang, T. Gan, H. Hu, Y. Zhang, Z. Feng, Z. Huang, Simultaneous growth strategy for constructing a Cu-Fe/carboxylate-decorated carbon composite with improved interface compatibility and charge transfer to boost the visible photocatalytic degradation of tetracycline, *Chem. Eng. J.* 448 (2022), 137608.
- [3] S. Park, S. Kim, Y. Yea, K. Saravanakumar, E. Lee, Y. Yoon, C.M. Park, Adsorptive and photocatalytic performance of cobalt-doped ZnTiO<sub>3</sub>/Ti<sub>3</sub>C<sub>2</sub>Tx MXene nanohybrids towards tetracycline: kinetics and mechanistic insight, *J. Hazard. Mater.* 443 (2023), 130165.
- [4] Q. Hua, X. Zhou, B. Zhang, M. Wang, J. Liu, Y. Wang, L. Jiang, Band modulation and interfacial engineering to generate efficient visible-light-induced bifunctional photocatalysts, *ACS Sustain. Chem. Eng.* 8 (2020) 2919–2930.
- [5] B. Zeng, S. Wang, Y. Gao, G. Li, W. Tian, J. Meeprasert, H. Li, H. Xie, F. Fan, R. Li, C. Li, Interfacial modulation with aluminum oxide for efficient plasmon-induced water oxidation, *Adv. Funct. Mater.* 31 (2021) 2005688.
- [6] Z. Zhou, Z. Shen, C. Song, M. Li, H. Li, S. Zhan, Boosting the activation of molecular oxygen and the degradation of tetracycline over high loading Ag single atomic catalyst, *Water Res.* 201 (2021), 117314.
- [7] C. Ling, X. Liu, H. Li, X. Wang, H. Gu, K. Wei, M. Li, Y. Shi, H. Ben, G. Zhan, C. Liang, W. Shen, Y. Li, J. Zhao, L. Zhang, Atomic-layered Cu<sub>5</sub> nanoclusters on FeS<sub>2</sub> with dual catalytic sites for efficient and selective H<sub>2</sub>O<sub>2</sub> activation, *Angew. Chem. Int. Ed.* 61 (2022), e202200670.
- [8] L. Su, P. Wang, J. Wang, D. Zhang, H. Wang, Y. Li, S. Zhan, J. Gong, Pt-Cu interaction induced construction of single Pt sites for synchronous electron capture and transfer in photocatalysis, *Adv. Funct. Mater.* 31 (2021) 2104343.
- [9] Y. Zhang, J. Liu, A. Moores, S. Ghoshal, Transformation of 6:2 fluorotelomer sulfonate by cobalt(II)-activated peroxydisulfate, *Environ. Sci. Technol.* 54 (2020) 4631–4640.
- [10] Y. Qian, D. Li, Y. Han, H.-L. Jiang, Photocatalytic molecular oxygen activation by regulating excitonic effects in covalent organic frameworks, *J. Am. Chem. Soc.* 142 (2020) 20763–20771.
- [11] H. Gu, X. Liu, X. Liu, C. Ling, K. Wei, G. Zhan, Y. Guo, L. Zhang, Adjacent single-atom irons boosting molecular oxygen activation on MnO<sub>2</sub>, *Nat. Commun.* 12 (2021) 5422.

- [12] Y. Yang, G. Zeng, D. Huang, C. Zhang, D. He, C. Zhou, W. Wang, W. Xiong, B. Song, H. Yi, S. Ye, X. Ren, In situ grown single-atom cobalt on polymeric carbon nitride with bidentate ligand for efficient photocatalytic degradation of refractory antibiotics, *Small* 16 (2020) 2001634.
- [13] L. Ding, M. Li, Y. Zhao, H. Zhang, J. Shang, J. Zhong, H. Sheng, C. Chen, J. Zhao, The vital role of surface Brönsted acid/base sites for the photocatalytic formation of free-OH radicals, *Appl. Catal. B-Environ.* 266 (2020), 118634.
- [14] D. Zhou, X. Xue, X. Wang, Q. Luan, A. Li, L. Zhang, B. Li, W. Dong, G. Wang, C. Hou, Ni, In co-doped ZnIn<sub>2</sub>S<sub>4</sub> for efficient hydrogen evolution: modulating charge flow and balancing H adsorption/desorption, *Appl. Catal. B-Environ.* (2022), 121337.
- [15] R. Yang, L. Mei, Y. Fan, Q. Zhang, R. Zhu, R. Amal, Z. Yin, Z. Zeng, ZnIn<sub>2</sub>S<sub>4</sub>-based photocatalysts for energy and environmental applications, *Small Methods* 5 (2021) 2100887.
- [16] T. Zhang, T. Wang, F. Meng, M. Yang, S. Kawi, Recent advances in ZnIn<sub>2</sub>S<sub>4</sub>-based materials towards photocatalytic purification, solar fuel production and organic transformations, *J. Mater. Chem. C* 10 (2022) 5400–5424.
- [17] C. Du, Q. Zhang, Z. Lin, B. Yan, C. Xia, G. Yang, Half-unit-cell ZnIn<sub>2</sub>S<sub>4</sub> monolayer with sulfur vacancies for photocatalytic hydrogen evolution, *Appl. Catal. B-Environ.* 248 (2019) 193–201.
- [18] J. Chen, K. Li, X. Cai, Y. Zhao, X. Gu, L. Mao, Sulfur vacancy-rich ZnIn<sub>2</sub>S<sub>4</sub> nanosheet arrays for visible-light-driven water splitting, *Mater. Sci. Semicond. Process* 143 (2022), 106547.
- [19] L. Tai, Y. Zhou, Creating zinc vacancy within 3D hierarchical ZnIn<sub>2</sub>S<sub>4</sub> particles for boosted photocatalytic performance towards H<sub>2</sub> evolution reaction, *Ceram. Int.* 47 (2021) 32218–32225.
- [20] Y. He, C. Chen, Y. Liu, Y. Yang, C. Li, Z. Shi, Y. Han, S. Feng, Quantitative evaluation of carrier dynamics in full-spectrum responsive metallic ZnIn<sub>2</sub>S<sub>4</sub> with indium vacancies for boosting photocatalytic CO<sub>2</sub> reduction, *Nano Lett.* 22 (2022) 4970–4978.
- [21] Y. Gao, B. Xu, M. Cherif, H. Yu, Q. Zhang, F. Vidal, X. Wang, F. Ding, Y. Sun, D. Ma, Y. Bi, Z. Xu, Atomic insights for Ag Interstitial/Substitutional doping into ZnIn<sub>2</sub>S<sub>4</sub> nanoplates and intimate coupling with reduced graphene oxide for enhanced photocatalytic hydrogen production by water splitting, *Appl. Catal. B-Environ.* 279 (2020), 119403.
- [22] F. Xing, Q. Liu, C. Huang, Mo-doped ZnIn<sub>2</sub>S<sub>4</sub> flower-like hollow microspheres for improved visible light-driven hydrogen, *Evol., Sol. RRL* 4 (2020) 1900483.
- [23] P. Wang, Z. Shen, Y. Xia, H. Wang, L. Zheng, W. Xi, S. Zhan, Atomic insights for optimum and excess doping in photocatalysis: a case study of few-layer Cu-ZnIn<sub>2</sub>S<sub>4</sub>, *Adv. Funct. Mater.* 29 (2019) 1807013.
- [24] E. Zhang, Q. Zhu, J. Huang, J. Liu, G. Tan, C. Sun, T. Li, S. Liu, Y. Li, H. Wang, X. Wan, Z. Wen, F. Fan, J. Zhang, K. Ariga, Visually resolving the direct Z-scheme heterojunction in CdS@ ZnIn<sub>2</sub>S<sub>4</sub> hollow cubes for photocatalytic evolution of H<sub>2</sub> and H<sub>2</sub>O<sub>2</sub> from pure water, *Appl. Catal. B-Environ.* 293 (2021), 120213.
- [25] J. Hu, T. Yang, J. Chen, X. Yang, J. Qu, Y. Cai, Efficient solar-driven H<sub>2</sub>O<sub>2</sub> synthesis in-situ and sustainable activation to purify water via cascade reaction on ZnIn<sub>2</sub>S<sub>4</sub>-based heterojunction, *Chem. Eng. J.* 430 (2022), 133039.
- [26] C.-Q. Li, X. Du, S. Jiang, Y. Liu, Z.-L. Niu, Z.-Y. Liu, S.-S. Yi, X.-Z. Yue, Constructing direct Z-scheme heterostructure by enveloping ZnIn<sub>2</sub>S<sub>4</sub> on CdS hollow cube for efficient photocatalytic H<sub>2</sub> generation, *Adv. Sci.* 9 (2022) 2201773.
- [27] Y. Li, D. Liao, T. Li, W. Zhong, X. Wang, X. Hong, H. Yu, Plasmonic Z-scheme Pt-Au/BiVO<sub>4</sub> photocatalyst: Synergistic effect of crystal-facet engineering and selective loading of Pt-Au cocatalyst for improved photocatalytic performance, *J. Colloid Interface Sci.* 570 (2020) 232–241.
- [28] Y. Nosaka, A.Y. Nosaka, Generation and detection of reactive oxygen species in photocatalysis, *Chem. Rev.* 117 (2017) 11302–11336.
- [29] P. Du, J. Wang, G. Sun, L. Chen, W. Liu, Hydrogen atom abstraction mechanism for organic compound oxidation by acetylperoxy radical in Co (II)/peracetic acid activation system, *Water Res* (2022), 118113.
- [30] J. Qi, X. Yang, P.-Y. Pan, T. Huang, X. Yang, C.-C. Wang, W. Liu, Interface engineering of Co(OH)<sub>2</sub> nanosheets growing on the KNbO<sub>3</sub> perovskite based on electronic structure modulation for enhanced peroxymonosulfate activation, *Environ. Sci. Technol.* 56 (2022) 5200–5212.
- [31] M. Frisch, G. Trucks, H. Schlegel, G. Scuseria, M. Robb, J. Cheeseman, G. Scalmani, V. Barone, G. Petersson, H. Nakatsuji, Gaussian 16 Revision C. 01. 2016, Gaussian Inc., Wallingford CT 421 (2016).
- [32] H. Ji, P. Du, D. Zhao, S. Li, F. Sun, E.C. Duin, W. Liu, 2D/1D graphitic carbon nitride/titanate nanotubes heterostructure for efficient photocatalysis of sulfamethazine under solar light: Catalytic “hot spots” at the rutile–anatase–titanate interfaces, *Appl. Catal. B-Environ.* 263 (2020), 118357.
- [33] X. Sun, X. Luo, S. Jin, X. Zhang, H. Wang, W. Shao, X. Wu, Y. Xie, Surface modification of ZnIn<sub>2</sub>S<sub>4</sub> layers to realise energy transfer-mediated photocatalysis, *Natl. Sci. Rev.* (9) (2022) nwac026.
- [34] Y. Wang, S. Jin, G. Pan, Z. Li, L. Chen, G. Liu, X. Xu, Zr doped mesoporous LaTaON<sub>2</sub> for efficient photocatalytic water splitting, *J. Mater. Chem. A* 7 (2019) 5702–5711.
- [35] M. Saito, C. Kura, H. Toriumi, S. Hinokuma, T. Ina, H. Habazaki, Y. Aoki, Formation of mobile hydridic defects in zirconium nitride films with n-type semiconductor properties, *ACS Appl. Electron. Mater.* 3 (2021) 3980–3989.
- [36] Q. Luan, X. Xue, R. Li, L. Gu, W. Dong, D. Zhou, X. Wang, B. Li, G. Wang, C. Hou, Boosting photocatalytic hydrogen evolution: Orbital redistribution of ultrathin ZnIn<sub>2</sub>S<sub>4</sub> nanosheets via atomic defects, *Appl. Catal. B-Environ.* 305 (2022), 121007.
- [37] S. Shen, L. Zhao, L. Guo, Morphology, structure and photocatalytic performance of ZnIn<sub>2</sub>S<sub>4</sub> synthesized via a solvothermal/hydrothermal route in different solvents, *J. Phys. Chem. Solids* 69 (2008) 2426–2432.
- [38] L. Ye, Z. Wen, Z. Li, H. Huang, Hierarchical architected ternary nanostructures photocatalysts with In(OH)<sub>3</sub> nanocube on ZnIn<sub>2</sub>S<sub>4</sub>/NiS nanosheets for photocatalytic hydrogen evolution, *Sol. RRL* 4 (2020) 2000027.
- [39] X. Peng, J. Li, L. Yi, X. Liu, J. Chen, P. Cai, Z. Wen, Ultrathin ZnIn<sub>2</sub>S<sub>4</sub> nanosheets decorating PPY nanotubes toward simultaneous photocatalytic H<sub>2</sub> production and 1,4-benzenedimethanol valorization, *Appl. Catal. B-Environ.* 300 (2022), 120737.
- [40] X. Peng, L. Ye, Y. Ding, L. Yi, C. Zhang, Z. Wen, Nanohybrid photocatalysts with ZnIn<sub>2</sub>S<sub>4</sub> nanosheets encapsulated UiO-66 octahedral nanoparticles for visible-light-driven hydrogen generation, *Appl. Catal. B-Environ.* 260 (2020), 118152.
- [41] M. Chen, C. Guo, S. Hou, J. Lv, Y. Zhang, H. Zhang, J. Xu, A novel Z-scheme AgBr/P-g-C<sub>3</sub>N<sub>4</sub> heterojunction photocatalyst: Excellent photocatalytic performance and photocatalytic mechanism for ephedrine degradation, *Appl. Catal. B-Environ.* 266 (2020), 118614.
- [42] B.B.Y. Hsu, C.M. Cheng, C. Luo, S.N. Patel, C. Zhong, H. Sun, J. Sherman, B.H. Lee, L. Ying, M. Wang, The density of states and the transport effective mass in a highly oriented semiconducting polymer: electronic delocalization in 1D, *Adv. Mater.* 27 (2015) 7759–7765.
- [43] L. Chen, J. Duan, P. Du, W. Sun, B. Lai, W. Liu, Accurate identification of radicals by in-situ electron paramagnetic resonance in ultraviolet-based homogenous advanced oxidation processes, *Water Res* (2022), 118747.
- [44] W. Liu, J. Ni, X. Yin, Synergy of photocatalysis and adsorption for simultaneous removal of Cr(VI) and Cr(III) with TiO<sub>2</sub> and titanate nanotubes, *Water Res.* 53 (2014) 12–25.
- [45] W. Liu, Y. Li, F. Liu, W. Jiang, D. Zhang, J. Liang, Visible-light-driven photocatalytic degradation of diclofenac by carbon quantum dots modified porous g-C<sub>3</sub>N<sub>4</sub>: Mechanisms, degradation pathway and DFT calculation, *Water Res.* 151 (2019) 8–19.
- [46] Y. Deng, Z. Zhou, H. Zeng, R. Tang, L. Li, J. Wang, C. Feng, D. Gong, L. Tang, Y. Huang, Phosphorus and potassium co-doped g-C<sub>3</sub>N<sub>4</sub> with multiple-locus synergies to degrade atrazine: Insights into the depth analysis of the generation and role of singlet oxygen, *Appl. Catal. B-Environ.* 320 (2023), 121942.
- [47] G. Li Puma, V. Puddu, H.K. Tsang, A. Gora, B. Toepfer, Photocatalytic oxidation of multicomponent mixtures of estrogens (estrone (E1), 17β-estradiol (E2), 17α-ethynylestradiol (EE2) and estril (E3)) under UVA and UVC radiation: Photon absorption, quantum yields and rate constants independent of photon absorption, *Appl. Catal. B-Environ.* 99 (2010) 388–397.
- [48] I. Grčić, G. Li Puma, Photocatalytic degradation of water contaminants in multiple photoreactors and evaluation of reaction kinetic constants independent of photon absorption, irradiance, reactor geometry, and hydrodynamics, *Environ. Sci. Technol.* 47 (2013) 13702–13711.
- [49] S. Jiao, S. Zheng, D. Yin, L. Wang, L. Chen, Aqueous photolysis of tetracycline and toxicity of photolytic products to luminescent bacteria, *Chemosphere* 73 (2008) 377–382.
- [50] J. Niu, S. Ding, L. Zhang, J. Zhao, C. Feng, Visible-light-mediated Sr-Bi<sub>2</sub>O<sub>3</sub> photocatalysis of tetracycline: Kinetics, mechanisms and toxicity assessment, *Chemosphere* 93 (2013) 1–8.
- [51] Y. Zhang, Z. Shen, Z. Xin, Z. Hu, H. Ji, Interfacial charge dominating major active species and degradation pathways: An example of carbon based photocatalyst, *J. Colloid Interface Sci.* 554 (2019) 743–751.
- [52] J. Yu, X. Wang, L. Chen, G. Lu, G. Shi, X. Xie, Y. Wang, J. Sun, Enhanced adsorption and visible-light photocatalytic degradation of toluene by CQDs/UiO-66 MOG with hierarchical pores, *Chem. Eng. J.* 435 (2022), 135033.
- [53] F. Dalanta, T.D. Kusworo, Synergistic adsorption and photocatalytic properties of AC/TiO<sub>2</sub>/CeO<sub>2</sub> composite for phenol and ammonia–nitrogen compound degradations from petroleum refinery wastewater, *Chem. Eng. J.* 434 (2022), 134687.
- [54] J.-C.E. Yang, Y. Lin, H.-H. Peng, B. Yuan, D.D. Dionysiou, X.-D. Huang, D.-D. Zhang, M.-L. Fu, Novel magnetic rod-like Mn-Fe oxycarbide toward peroxymonosulfate activation for efficient oxidation of butyl paraben: radical oxidation versus singlet oxygenation, *Appl. Catal. B-Environ.* 268 (2020), 118549.
- [55] F. Pan, H. Ji, P. Du, T. Huang, C. Wang, W. Liu, Insights into catalytic activation of peroxymonosulfate for carbamazepine degradation by MnO<sub>2</sub> nanoparticles in-situ anchored titanate nanotubes: mechanism, ecotoxicity and DFT study, *J. Hazard. Mater.* 402 (2021), 123779.